Opto-Electronic Advances

ISSN 2096-4579 CN 51-1781/TN

Resonantly enhanced second- and third-harmonic generation in dielectric nonlinear metasurfaces

Ji Tong Wang, Pavel Tonkaev, Kirill Koshelev, Fangxing Lai, Sergey Kruk, Qinghai Song, Yuri Kivshar and Nicolae C. Panoiu

Citation: Wang JT, Tonkaev P, Koshelev K, et al. Resonantly enhanced second- and third-harmonic generation in dielectric nonlinear metasurfaces. *Opto-Electron Adv* **7**, 230186(2024).

https://doi.org/10.29026/oea.2024.230186

Received: 10 October 2023; Accepted: 4 February 2024; Published online: 15 May 2024

Opto-Electronic Advances

Article

May 2024, Vol. 7, No. 5

DOI: 10.29026/oea.2024.230186

Resonantly enhanced second- and third-harmonic generation in dielectric nonlinear metasurfaces

Ji Tong Wang[1], Pavel Tonkaev[2], Kirill Koshelev[2], Fangxing Lai[3], Sergey Kruk[2], Qinghai Song[3], Yuri Kivshar[2] and Nicolae C. Panoiu[1,4]*

Nonlinear dielectric metasurfaces provide a promising approach to control and manipulate frequency conversion optical processes at the nanoscale, thus facilitating both advances in fundamental research and the development of new practical applications in photonics, lasing, and sensing. Here, we employ symmetry-broken metasurfaces made of centrosymmetric amorphous silicon for resonantly enhanced second- and third-order nonlinear optical response. Exploiting the rich physics of optical quasi-bound states in the continuum and guided mode resonances, we comprehensively study through rigorous numerical calculations the relative contribution of surface and bulk effects to second-harmonic generation (SHG) and the bulk contribution to third-harmonic generation (THG) from the meta-atoms. Next, we experimentally achieve optical resonances with high quality factors, which greatly boosts light-matter interaction, resulting in about 550 times SHG enhancement and nearly 5000-fold increase of THG. A good agreement between theoretical predictions and experimental measurements is observed. To gain deeper insights into the physics of the investigated nonlinear optical processes, we further numerically study the relation between nonlinear emission and the structural asymmetry of the metasurface and reveal that the generated harmonic signals arising from linear sharp resonances are highly dependent on the asymmetry of the meta-atoms. Our work suggests a fruitful strategy to enhance the harmonic generation and effectively control different orders of harmonics in all-dielectric metasurfaces, enabling the development of efficient active photonic nanodevices.

Keywords: second-harmonic generation; third-harmonic generation; bound state in the continuum; guided mode resonance; all-dielectric metasurfaces; nonlinear optics

Wang JT, Tonkaev P, Koshelev K et al. Resonantly enhanced second- and third-harmonic generation in dielectric nonlinear metasurfaces. *Opto-Electron Adv* **7**, 230186 (2024).

Introduction

Optical metasurfaces, ultrathin artificial periodic nanostructures, have demonstrated a remarkable potential for the control of light properties, including phase, amplitude, and polarization. They have been instrumental in spurring advances in fundamental research and development of new practical applications from mid-IR to UV

[1]Department of Electronic and Electrical Engineering, University College London, London WC1E 7JE, United Kingdom; [2]Nonlinear Physics Center, Research School of Physics, Australian National University, Canberra ACT 2601, Australia; [3]Ministry of Industry and Information Technology Key Lab of Micro-Nano Optoelectronic Information System, Guangdong Provincial Key Laboratory of Semiconductor Optoelectronic Materials and Intelligent Photonic Systems, Harbin Institute of Technology, Shenzhen 518055, China; [4]Wuzhen Laboratory, EGO Wuzhen Digital Economy Industrial Park, No. 925 Daole Road, Tongxiang, China.

*Correspondence: NC Panoiu, E-mail: n.panoiu@ucl.ac.uk

Received: 10 October 2023; Accepted: 4 February 2024; Published online: 15 May 2024

wavelengths[1–3]. Compared to traditional bulky metamaterials[4,5], two-dimensional (2D) metasurfaces offer remarkable advantages stemming from feasibility of their nanofabrication and high optical throughput. These unique features have facilitated rapid technological advances and development of various applications, including integrated optics[6], sensing[7,8], and information processing[9,10]. A notable characteristic of metasurfaces is their ability to create local optical field enhancement and confinement. This created a prominent platform of nonlinear optical metasurfaces[11,12]. Nonlinear metasurfaces provide enhanced and controlled frequency conversion in processes such as second-[13,14], third-[15,16] and higher-harmonics generation[17]. Importantly, metasurfaces relax the constraints imposed by phase-matching conditions, required to be satisfied when nonlinearly interacting waves propagate in three-dimensional (3D) bulk optical media.

Generally, optical metasurfaces can be classified into two categories based on their constituent elements: plasmonic metasurfaces that rely on metallic resonators[18,19] and dielectric metasurfaces comprising of dielectric materials with high index of refraction[20,21]. Plasmonic metasurfaces can induce remarkably strong local field enhancements, usually at the plasmon-resonance frequencies of their constituent nanoparticles, but their use in nanophotonic applications has been hindered by large optical losses and low damage thresholds. On the other hand, high-refractive-index dielectric metasurfaces have much lower dissipative loss, albeit with a weaker field enhancement.

Recently, it has been shown that optically resonant all-dielectric metasurfaces based on guided mode resonances (GMRs)[22–24] make it possible to achieve large quality-(Q) factor resonant effects and enable effective optical elements in applications, such as wave-front shaping[25], sensing[26], and harmonic generation[23,27–29]. The underlying physics of the collective phenomenon of GMRs in metasurfaces with a periodic lattice can be explained by the propagation of in-plane diffractive modes under the condition of total internal reflection. However, unlike the case of guided modes of photonic crystal slab waveguides, these diffractive modes can couple to the radiation continuum, so that optical energy can leak into the free space. Moreover, a recently revealed physical mechanism, responsible for the generation of so-called bound states in the continuum (BICs)[30–33], suggests a novel method to achieve a strong coupling between light and certain photonic systems. Ideally, BICs are completely decoupled from the radiative modes of the continuum and thus possess infinitely large radiative Q-factor (or, equivalently, zero linewidth). Due to surface roughness, material loss, inherent fabrication imperfections, and other perturbations, in practical devices, BICs are characterized by limited but large Q-factor. The spectral response of these quasi-BICs is usually described by Fano resonances with an asymmetric line shape[34]. More recently, it was shown that dielectric metasurfaces with broken in-plane inversion symmetry can possess sharp resonances with extremely large Q-factor driven by symmetry-protected BICs at high symmetry points[35], such as the Γ point. The dependence of the Q-factor of BICs on the geometric asymmetry of meta-atoms allows for flexibility in the design of metasurfaces supporting high-Q resonances and to an effective control of the strength of light-matter interaction within a wide spectral range. Spurred by these ideas, BICs have been intensively studied not only in linear optics applications, including vortex beam generation[36,37] and light guiding photonic devices[38,39], but also in relation to a plethora of nonlinear optical effects, such as giant harmonic generation[15,28,40–42] and self-action effects[43,44].

In this paper, we propose an amorphous silicon nonlinear metasurface utilizing the versatile physics of both guided mode resonances and symmetry-protected bound states in the continuum to enhance and tailor the second- and third-order nonlinear optical response of the metasurface. Compared to existing works on using GMRs and BICs to enhance second- and third-order nonlinear interactions in metasurfaces[15,28,29,41,42], our study goes further and more in-depth in the following important ways. i) Both GMRs and BICs were utilized in our work and the enhancement of nonlinear optical effects from asymmetric metasurfaces were compared in terms of their distinct physical mechanisms. ii) Different from other reported results, whereby the attention was focused mostly on one particular harmonic order, we showed in this study large enhancement of both SHG (550 times enhancement) and THG (5000-fold enhancement) from the same amorphous silicon metasurface. iii) A comprehensive computational analysis of the SHG from metasurfaces made of centrosymmetric amorphous silicon was performed via a rigorous theoretical model, which considered both surface and bulk contributions to the nonlinear optical response.

More specifically, to enable the optical coupling

between the BICs and the radiative states in the continuum, we introduce a certain degree of asymmetry to the constituting meta-atoms of the metasurface, comprising a pair of silicon bars. The corresponding fabricated metasurface is thus characterized by a certain asymmetry parameter. The experiments show that the asymmetric metasurface produces a large enhancement of the SHG with a maximum measured enhancement of 550, whereas the THG increases by a maximum of 5000, as compared to that of an amorphous silicon slab with the same thickness as that of the metasurface. In addition, we perform a comprehensive numerical analysis of the surface and bulk contributions to the SHG, as well as of the bulk contribution to the third-order nonlinear interaction, when the meta-atoms of the metasurface are made of centrosymmetric amorphous silicon. The predictions of our computational analysis are compared to the corresponding experimentally measured physical quantities and good agreement is observed. In particular, we numerically investigate the dependence of the intensity of the nonlinear signals on the structural asymmetry of the nonlinear metasurface. Some promising potential applications of our proposed metasurface to the effective control and manipulation of both SHG and THG from dielectric metasurfaces are discussed.

Metasurface design and methods

We study a nonlinear metasurface with a square-lattice arrangement of unit elements made of amorphous silicon, placed on top of a glass substrate, as illustrated in Fig. 1. The unit cell is composed of a pair of asymmetric amorphous silicon bars with width w and $w-\Delta w$, respectively, while the length and thickness of the two bars are identical. The period of the metasurface array is $\Lambda = 830$ nm. To quantify the asymmetric nature of the meta-atom, we define an asymmetry parameter as $\alpha = \Delta w/w$. The asymmetry parameter of the meta-atom offers the degree of freedom to control the linear and nonlinear optical responses of the metasurface and its resonant enhancement. In the case of $\alpha = 0$, the metasurface has in-plane inversion symmetry but lacks C_4 rotational symmetry, thus permitting different sets of resonances under x/y-polarized plane-wave excitation. The two bars in each unit cell placed along the x-direction are 380 nm apart and the length (along the x-axis), width (along the y-axis), and thickness of the two bars are 630 nm, 260 nm, and 600 nm, respectively.

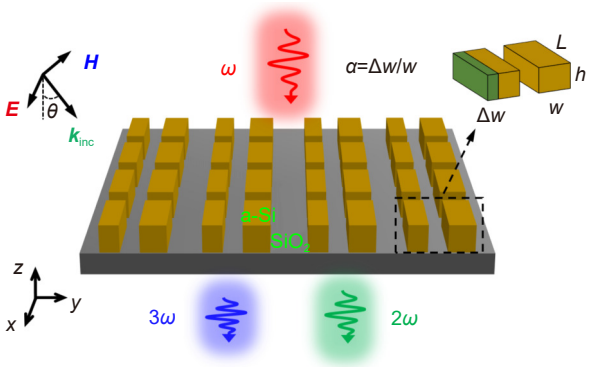

Fig. 1 | Enhanced second- and third-harmonic generation from an asymmetric nonlinear metasurface. Schematics of a nonlinear metasurface consisting of a periodic array of pairs of amorphous silicon bars placed on top of a glass substrate. The geometric asymmetry parameter, α, of the meta-atom is defined as $\alpha = \Delta w/w$.

The proposed nonlinear optical metasurface was analyzed theoretically and investigated experimentally as well. Both linear and nonlinear optical responses of the metasurface have been computed using full-wave numerical simulations. In particular, we used a frequency-domain solver, part of COMSOL Multiphysics[45], a commercially available software that implements the finite-element method. For the eigenmode analysis and near-field distribution of the optical modes, the eigenmode solver of COMSOL Multiphysics has been employed. All computations pertaining to the amorphous silicon metasurface placed on a semi-infinite glass substrate were performed for a single unit cell by imposing Bloch periodic boundary conditions along x and y directions, so that effectively an infinite periodic metasurface was modelled. Moreover, two perfectly-matched layers were placed transverse to the z-axis, so as to absorb outgoing waves and minimize reflections. The linear spectra computed using COMSOL Multiphysics were validated by comparing them with the spectra determined with the rigorous coupled wave analysis method implemented in Synopsys' [46] DiffractMOD. The frequency dispersion of the complex index of refraction of amorphous silicon[47] and glass[48] (CDGM – K (Crown), D-K9) was taken into consideration by fitting the experimental data. In the linear simulations, linearly polarized plane-waves (wave intensity $I_0 = 145.2\ \mathrm{MW/cm^2}$) were employed as excitation source, whereas the nonlinear optical emission from the metasurface was determined under the assumption of undepleted pump approximation that neglects the back-conversion of generated harmonic signal to the pump frequency. The computational procedure comprised three steps: first, the distribution of the near-field in the

amorphous silicon nanostructure was obtained under the plane-wave excitation conditions at the pump wavelength. In the second step, we computed the nonlinear polarization induced in the nonlinear dielectric scatterer using the optical field at the fundamental frequency (FF) calculated in the first step. Finally, in the last step, we used as sources at either the second harmonic (SH) or third harmonic (TH) the nonlinear polarizations computed at the preceding step and determined the generated optical field at the higher harmonics.

In this work, the nonlinear optical response from the dielectric metasurface includes both second- and third-order frequency conversion processes. Regarding the SHG process, it represents a quadratic nonlinear optical interaction, and therefore, under the electric dipole approximation, it is forbidden in a centrosymmetric optical medium, that is a medium whose atomic structure is invariant upon inversion symmetry transformation. As a consequence, we employed a widely used model for SHG from centrosymmetric media to describe the second-order nonlinear optical process, whereby in the bulk of the meta-atoms the SHG is due to higher-order multipoles[49,50], whereas the surface response is treated in the dipole approximation as at the surface of the meta-atoms the inversion symmetry is broken. More specifically, in this model, the nonlinear polarization consists of a dipole-allowed (local) surface contribution arising from the locally broken inversion symmetry at the interface between the centrosymmetric material and the environment, and a (nonlocal) bulk contribution induced inside the nonlinear optical medium caused by the spatial variation of the optical field. As a result, the surface and bulk contributions to the nonlinear optical response at the SH from amorphous silicon meta-atoms can be described *via* two nonlinear polarizations as:

$$\boldsymbol{P}^{\mathrm{s}(2)}(2\omega;\boldsymbol{r}) = \varepsilon_0\chi^{\mathrm{s}(2)} : \boldsymbol{E}(\omega;\boldsymbol{r})\boldsymbol{E}(\omega;\boldsymbol{r})\boldsymbol{\delta}(\boldsymbol{r}-\boldsymbol{r}_{\mathrm{s}}), \quad (1a)$$

$$\begin{aligned}\boldsymbol{P}_i^{\mathrm{b}(2)}(2\omega;\boldsymbol{r}) = {}& \gamma\nabla_i\left[\boldsymbol{E}(\omega;\boldsymbol{r})\cdot\boldsymbol{E}(\omega;\boldsymbol{r})\right] \\ & + \beta\left[\nabla\cdot\boldsymbol{E}(\omega;\boldsymbol{r})\right]E_i(\omega;\boldsymbol{r}) + \zeta E_i(\omega;\boldsymbol{r}) \\ & \nabla_i E_i(\omega;\boldsymbol{r}) + \delta'\left[\boldsymbol{E}(\omega;\boldsymbol{r})\cdot\nabla\right]E_i(\omega;\boldsymbol{r}), \quad (1b)\end{aligned}$$

where $\boldsymbol{P}^{\mathrm{s}(2)}$ and $\boldsymbol{P}^{\mathrm{b}(2)}$ denote the surface and bulk quadratic nonlinear polarizations, respectively, $\boldsymbol{E}(\omega;\boldsymbol{r})$ is the electric field at the FF, $\boldsymbol{r}_s$ defines the surface of the nonlinear medium, $\chi^{\mathrm{s}(2)}$ is the surface nonlinear susceptibility tensor, and γ, β, ζ, and δ' are material parameters (nonlinear susceptibilities) characterizing the electric quadrupole and magnetic dipole contributions to the bulk nonlinear polarization.

Owing to the isotropic mirror symmetric property of the interface between amorphous silicon and environment, the second-order surface susceptibility tensor $\chi^{\mathrm{s}(2)}$ has only three independent, non-vanishing components: $\chi^{\mathrm{s}(2)}_{\perp\perp\perp}$, $\chi^{\mathrm{s}(2)}_{\perp\parallel\parallel}$, and $\chi^{\mathrm{s}(2)}_{\parallel\perp\parallel} = \chi^{\mathrm{s}(2)}_{\parallel\parallel\perp}$, where the symbols $\perp$ and $\parallel$ denote the normal and tangential directions with respect to the interface, respectively. For amorphous silicon, the susceptibility components measured at $\lambda = 800$ nm are[51] $\chi^{\mathrm{s}(2)}_{\perp\perp\perp} = 150\times10^{-22}\ \mathrm{m^2V^{-1}}$ and $\chi^{\mathrm{s}(2)}_{\parallel\perp\parallel} = \chi^{\mathrm{s}(2)}_{\parallel\parallel\perp} = 8.2\times10^{-22}\ \mathrm{m^2V^{-1}}$, whereas $\chi^{\mathrm{s}(2)}_{\perp\parallel\parallel}$ can be neglected as compared to the other components, as predicted by most theoretical models[52,53]. In the case of the bulk part of nonlinear susceptibility in Eq. (1b), the second term vanishes as $\nabla\cdot\boldsymbol{E}(\omega;\boldsymbol{r}) = 0$ in homogeneous media (meaning that the FF optical field is a transverse field) and the ζ parameter of the third term, which accounts for the anisotropy of the material nonlinearity, can also be neglected because of the isotropic structure of amorphous silicon. Concerning the δ' term in Eq. (1b), theoretical models[54] predict that it can be neglected, too. Under these circumstances, in our numerical simulation settings we set β, ζ, and δ' to be zero. As a result, the first term in Eq. (1b) solely determines the second-order nonlinear bulk polarization. The value of γ, measured at $\lambda = 800$ nm[51], is $\gamma = 3.1\times10^{-22}\ \mathrm{V^{-1}}$.

In addition to the quadratic frequency conversion process, third-order nonlinear interaction from the proposed bar-shaped amorphous silicon metasurface was also studied to determine the conditions in which it can be enhanced via the excitation of GMRs and/or BICs. The bulk nonlinear polarization induced at the TH can be expressed as:

$$\boldsymbol{P}_i^{(3)}(3\omega;\boldsymbol{r}) = \varepsilon_0\chi^{(3)}E_i(\omega;\boldsymbol{r})\left[\boldsymbol{E}(\omega;\boldsymbol{r})\cdot\boldsymbol{E}(\omega;\boldsymbol{r})\right], \quad (2)$$

where $\chi^{(3)}$ is the nonlinear susceptibility. Since amorphous silicon is a homogeneous medium, the nonlinear susceptibility $\chi^{(3)}$ is a scalar quantity. The value of $\chi^{(3)}$ was determined at the telecommunication wavelength (1550 nm) by measuring the Kerr coefficient, n_2, and the two-photon absorption (TPA) coefficient, β_{TPA}. These coefficients are related to the third-order susceptibility via the relations $n_2 = 3\chi'^{(3)}/4\varepsilon_0cn^2$ and $\beta_{\mathrm{TPA}} = 3\omega\chi''^{(3)}/2\varepsilon_0c^2n^2$, where $\chi'^{(3)}$ and $\chi''^{(3)}$ are the real and imaginary parts of $\chi^{(3)}$, respectively, and n is the index of refraction of the medium. For amorphous silicon[55], $n_2 = 2.1\times10^{-17}\ \mathrm{m^2W^{-1}}$ and $\beta_{\mathrm{TPA}} = 0.25\ \mathrm{cmGW^{-1}}$.

Note that in our numerical simulations we do not incorporate the frequency dispersion of second- (both surface and bulk terms) and third-order (bulk term) nonlinearity coefficients of amorphous silicon due to the lack of experimental data. Despite this fact, our analysis still provides accurate insights into the underlying physics of SHG and THG in the nonlinear metasurface as the frequency dispersion of the optical nonlinearity is weak. This is so because our experimental and theoretical study is performed for frequencies that are far from the intrinsic resonance frequencies of the optical medium (amorphous silicon).

The detailed process of sample fabrication includes the deposition of amorphous Si membrane, the electron-beam lithography, and the reactive ion etching. Specifically, a 600 nm amorphous Si film is deposited onto the SiO_2 substrate and then covered by a 30 nm Cr film as a hard mask in an electron beam evaporator (deposition rate 0.5 Å/s (1 Å=10^{-10} m), Syskey Tech). An 80 nm PMMA film is spin-coated and patterned by electron-beam lithography (Raith E-line, 30 kV). The designed nanostructures are achieved in PMMA film after developing in MIBK/IPA solution for 30 s at 0 °C. Then the pattern is transferred to the Cr film and eventually to the Si membrane via two reactive ion etching processes in an inductively coupled plasma etcher (Plasmalab System 100 ICP180). The Si metasurfaces are finally obtained by removing the Cr mask with chromium etchant.

Although in this work we focus on the theoretical analysis of the optical response of a dielectric metasurface with broken inversion symmetry, we validate our main conclusions by measuring key physical quantities, such as the linear transmittance spectra and emitted nonlinear signals at the SH and TH. The experimental measurements are performed for a metasurface with asymmetry parameter $\alpha = 0.075$. The linear measurements are performed with a home-made microscope system. The linearly polarized (LP) output from a tunable laser (Yenista TUNICS-T100S-HP) is collimated and normally focused onto the metasurface sample through an objective lens. The transmitted light is collected by the second objective lenses and directed to a photodetector (New Focus 1800FC) by an optical lens. In this case, due to in-plane inversion symmetry breaking, it is expected that the designed metasurface supports both GMRs and quasi-BICs with high Q-factors, enabling significant enhancement of light-matter interaction. For nonlinear measurements, we used a laser system consisting of a 1030 nm laser (Ekspla Femtolux 3) and an optical parametric amplifier (OPA, MIROPA from Hotlight Systems). The laser has a pulse duration of 5.76 ps and a repetition rate of 5.14 MHz. The OPA produces mid-IR radiation with power of 40 mW and wavelength range from 1500 nm to 1750 nm. The laser was focused by a CaF_2 lens with focus distance of 40 mm. The harmonics signal was collected in transmission with a Mitutoyo MPlan Apo X50 0.42 NA microscope objective and detected with a Peltier-cooled spectrometer Ocean Optics QE Pro.

Results and discussion

In this section, we present the results of our experimental and theoretical investigations of both the linear and nonlinear optical response of the dielectric metasurface. We consider both second- and third-harmonic processes, with a special focus being placed on understanding the mechanisms that lead to the enhancement of these nonlinear optical interactions.

Linear optical response of the metasurface

The efficiency of the frequency conversion processes in a nonlinear metasurface is chiefly determined by the distribution of the optical near-field around the meta-atoms and the strength of the light-matter interaction at the FF. Therefore, we start our investigations with the numerical calculation of linear transmittance, by sweeping the asymmetry parameter α and the angle of incidence θ and looking for resonances of the optical system as well as their linewidth and frequency dispersion properties. In these calculations, we used the rigorous coupled-wave analysis implemented in Synopsys's DiffractMOD. The optical excitation is a plane-wave linearly polarized either along the long side of the bars (x-axis) or along their short side (y-axis).

In the case of x-polarized, normally incident plane-wave, as illustrated in Fig. 2(a), all spectral resonances are blue-shifted as the structural asymmetry parameter α increases from 0 to 1. When α becomes vanishingly small, the linewidth of the two sharp resonances at around 1780 nm vanishes so that their Q-factors diverge. This is a key feature of symmetry-protected BICs at the Γ point. Furthermore, based on the diffraction theory for 2D periodic structures, below the first Bragg-diffraction limit frequency, $f_B = c/n_{sub}\Lambda = 240.8$ THz ($\lambda_B = c/f_B = 1245$ nm), where c is the speed of light in vacuum and n_{sub} is the index of refraction of the substrate (glass), only the zeroth-order diffraction channel

exists. For our design, the frequency of the two resonances is just below this diffraction limit, thus satisfying a key prerequisite for the existence of BICs. To utilize the physics of BICs, in-plane inversion symmetry is broken by reducing the width of one of the amorphous silicon bar pairs. The BICs generated *via* this procedure are expected to be characterized by a large *Q*-factor, chiefly due to the fact that radiative processes are suppressed.

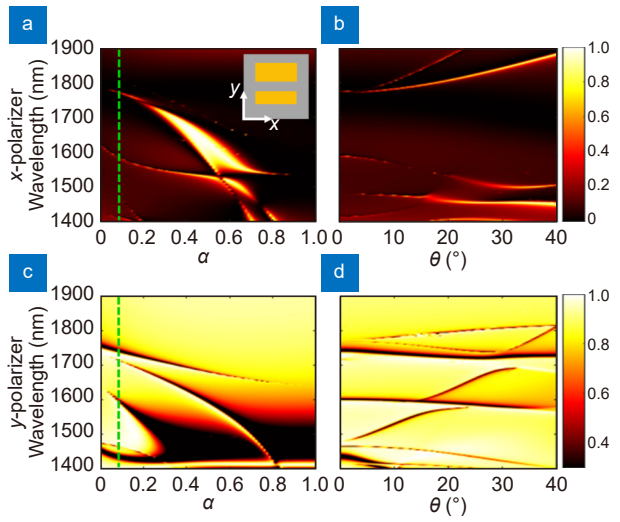

Fig. 2 | Simulated linear transmission spectra of the metasurface. (**a**) Dependence of transmission on the asymmetry parameter α under normal incidence and for *x*-polarized plane-wave excitation. The green dashed line corresponds to α = 0.075. (**b**) Dependence of transmission on the angle of incidence θ, determined for α = 0.075 and for *x*-polarized plane-wave excitation. (**c**, **d**) Same as in (a) and (b), respectively, but determined for *y*-polarized plane-wave excitation.

In addition to BICs, GMR-type resonances are also a promising way to realize metasurfaces that possess optical resonances with a large *Q*-factor. This is achieved through the coupling of diffracted waves propagating in the plane of the metasurface to the radiation continuum. For normal incidence, GMRs in two-dimensional periodic structures exist if the nanostructure satisfies the phase-matching condition for total internal reflection[24,56]: $\max\left[n_{\mathrm{air}}, n_{\mathrm{sub}}\right] \le \lambda \left|\sqrt{m^2+n^2}/\Lambda\right| < n_{\mathrm{eff}}$, where n_{air} is the index of refraction of air, λ is the working wavelength, m and n are integers defining the diffraction order, Λ is the lattice period, and n_{eff} is the effective index of refraction of the unit cell. Using the value of n_{eff} calculated from the filling factor of the amorphous silicon in our designed metasurface[56], we determined that this critical condition defining the first diffraction order is satisfied in the wavelength range considered in this work, i.e., spanning the 1400 nm to 1900 nm domain. As a result, a GMR with a large *Q*-factor can be observed in the case of a symmetric meta-atom ($\alpha = 0$) at 1622 nm under *x*-polarized normal incidence, as per Fig. 2(a). It should be noted that the linewidth of quasi-BICs is inversely proportional to the structural asymmetry parameter α, whereas that of the GMR is practically independent on α.

To gain a deeper understanding of the physical properties of BIC-type and GMR-type resonances, we further calculate the angle-dependent transmission map under the condition of $\alpha = 0.075$, denoted as a green dashed line in Fig. 2(a), where the incident beam is polarized along the *x*-axis (s-polarized wave) and the angle of incidence is varied by changing the wavevector k_y ($k_x = 0$). The corresponding results are shown in Fig. 2(b). Interestingly enough, the spectral locations of the two quasi-BICs diverge from each other as the angle of incidence increases, whereas the resonance wavelength of the GMR decreases monotonously as the angle of incidence θ increases up to about $\theta \approx 30°$.

Due to the lack of C_4 rotational symmetry of the metasurface with bar-shaped elements in the unit cell, it is also relevant to study the linear optical response of the metasurface under s-polarized plane-wave excitation; the results of this analysis are summarized in Fig. 2(c) and 2(d). In the case when the meta-atom possesses in-plane inversion symmetry ($\alpha = 0$), two BICs with vanishingly small linewidth are found at wavelengths of 1640 nm and 1736 nm, and a GMR with relatively large linewidth is found at 1760 nm. The evolution of these three resonances with the variation of θ, at α = 0.075, is shown in Fig. 2(d), whereby the incident plane-wave is polarized along the *y*-axis (*s*-polarized plane-wave). The physical properties of the optical resonances under *y*-polarization of the incident plane-wave are similar to those in the *x*-polarized case, so that they will not be discussed in detail here. However, one fact that does need to be mentioned is that the resonant behavior of the quasi-BIC around 1715 nm at $\theta = 0°$ in Fig. 2(d) weakens considerably when the angle of incidence increases beyond 2°. This finding can be explained by the large radiative losses into the free space when the incident wave is off Γ-point. We can thus conclude from the linear optical transmission maps for both polarizations that the metasurface possesses both BICs and high-*Q* GMRs. Importantly, the resonant behavior of these optical modes can be controlled by varying the asymmetry parameter and the angle of incidence of the plane-wave excitation.

The analysis of the modes of the metasurface can provide valuable information regarding the efficiency of the interaction between the incoming light and the metasurface. To this end, we considered the cubic lattice with asymmetric unit cell ($\alpha = 0.075$) and calculated its eigenmodes using the finite-element method implemented in COMSOL Multiphysics. Due to the absence of in-plane inversion symmetry of the unit cell, here we investigate the band structure of the metasurface in the reciprocal lattice, along two paths in the k-space: $(0,0) \rightarrow (0,\pi/\Lambda)$ and $(0,0) \rightarrow (\pi/\Lambda,0)$. The results of this analysis are summarized in Fig. 3(a) and 3(b). In the band diagrams presented in these figures, only modes with Q-factors that are larger than 50 are presented, as only these modes would lead to a significantly enhanced light-matter interaction. In addition, this facilitates a comparison with the results revealed by the transmission spectral maps presented in Fig. 2.

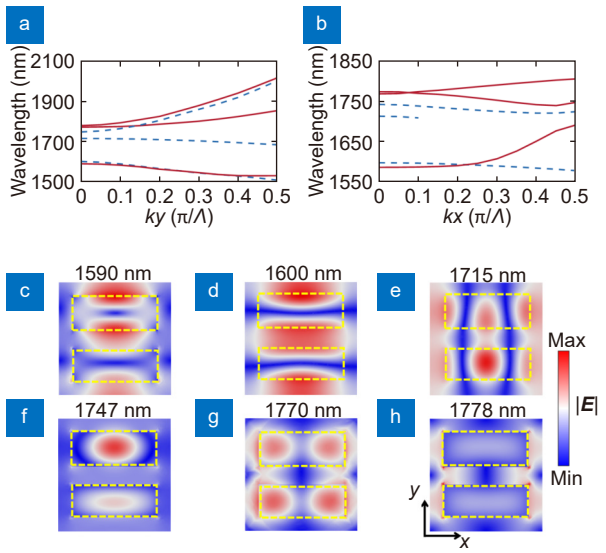

Fig. 3 | Eigenmode analysis in case of α = 0.075. Band diagrams with respect to (**a**) k_y and (**b**) k_x. Only modes with Q-factors larger than 50 are included. Red solid (blue dotted) lines are modes excited by x-polarized (y-polarized) plane-waves. (**c–h**) In-plane electric field profiles of the eigenmodes at the Γ point, presented in order of increasing wavelength. The yellow dashed lines indicate the interfaces between amorphous silicon and air.

The calculated eigenmodes present in the linear transmission spectra are classified according to the polarization of the incident plane-wave, which was either along x- or y-axis. As can be observed from Fig. 2(b) and Fig. 3(a), in the case of the eigenmodes that can couple to x-polarized plane waves, there is a good agreement between the frequency dispersion of resonances presented in the angle-resolved transmission map and in the eigenmode spectra (red solid lines). A similarly good agreement can be observed in the other case (eigenmodes that couple with y-polarized plane-waves), whereby the bands in the dispersion map in Fig. 2(d) agree well with the photonic bands indicated as blue dotted lines in Fig. 3(b). Moreover, Fig. 3(c–h) show the spatial distribution of the electric near-field ($x-y$ plane) within the unit cell in the middle cross-section of the amorphous silicon bar pairs at the Γ point. The field profiles correspond to the increasing wavelength of the optical eigenmodes. Due to the asymmetric nature of the unit cell of the dielectric metasurface, it is expected that the electric field patterns also present asymmetric features, which accounts for the optical coupling into free space of BIC-type resonances.

Since the rate at which a resonance of the optical metasurface radiates into the continuum is quantified by the Q-factor, it is particularly relevant to evaluate the Q-factor of the resonances. This physical quantity is important not just for the characterization of the light-matter interaction in the linear regime, but it also plays a critical role in the nonlinear optical regime whereby it is related to the optical near-field enhancement. We computed the dependence of the Q-factor at the Γ point of various resonances on the asymmetry parameter α of the meta-atom by using the eigenmode solver in COMSOL Multiphysics, the results of these calculations being shown in Fig. 4. It can be seen in this figure that for a symmetric metasurface ($\alpha = 0$), for both polarizations of the incident plane-wave, there are eigenmodes with diverging Q-factors, implying that they are of a BICs nature. With the increase of the metasurface asymmetry parameter, the Q-factor of BICs decreases rapidly, which, as illustrated in Fig. 2(a) and 2(c), results in a considerable broadening of the corresponding linewidth. By contrast, the Q-factor of the GMRs is finite for all values of the asymmetry parameter and, as illustrated by the practically flat curves in Fig. 4, shows a weak dependence on the structural asymmetry parameter. Moreover, for the sake of completeness, for both BIC- and GMR-type resonances, we provide here the calculated resonance wavelengths and the corresponding Q-factors corresponding to the asymmetry parameter value ($\alpha = 0.075$) at which the amorphous silicon metasurface was experimentally characterized: λ=1590 nm (Q = 2176, GMR), λ=1600 nm (Q = 400, BIC), λ=1715 nm (Q = 4723, BIC), λ=1747 nm (Q = 230, GMR), λ=1770 nm (Q = 1562, BIC), and λ=1778 nm (Q = 4965, BIC).

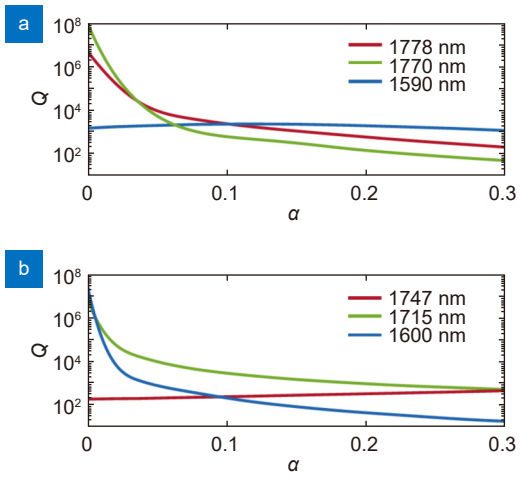

Fig. 4 | Simulated dependence of *Q*-factor of the metasurface eigenmodes on the structural asymmetry parameter α for modes excited by (**a**) *x*-polarized and (**b**) *y*-polarized incident plane-waves. The calculations are performed at the Γ point.

One key feature of BIC modes is that they have a topological nature, meaning that they are characterized by a topological invariant called topological charge. By using a well-known approach based on the dependence of the phase of the of the mode polarization in the *k*-space, we have found out that the topological charge of the BICs at 1600 nm, 1715 nm, 1770 nm, and 1778 nm is −1, 1, 1, and −1, respectively.

Enhanced SHG and THG from nonlinear metasurfaces

We now move on to the nonlinear optical response of the amorphous silicon metasurface and investigate the relationship between the excitation of BIC- or GMR-type resonances and the enhancement of nonlinear optical interactions. To illustrate the agreement between predictions of rigorous computational analysis and experimental results, we have fabricated an amorphous silicon metasurface corresponding to $\alpha = 0.075$. Figure 5(a) presents a scanning electron microscope (SEM) image of the fabricated periodic pattern, showing the symmetry-broken feature of the square array dielectric metasurface. Before we characterized the nonlinear enhancement effects in the asymmetric metasurface, we measured the linear transmissivity spectra (see Fig. 5(b)) under *x*-polarized illumination, determined over a spectral interval ranging from 1500 nm to 2000 nm. As illustrated in Fig. 5(b), the transmission spectra obtained from experiments and simulation show similar features for wavelengths ranging from 1500 nm to 2000 nm. Particularly, a resonance with an asymmetric line shape can be observed at 1620 nm in the experimentally determined spectrum (marked by a purple arrow), corresponding to the sharp resonance seen at 1590 nm in the simulated transmission spectrum, the difference between the two values being less than 2%. This resonance is used to demonstrate further the dependence of the transmitted nonlinear optical signals at the SH and TH on the pump power at the FF. For the numerically calculated transmission spectrum, two more sharp resonances with extremely narrow linewidth exist at around 1780 nm. The fact that the signature of these extremely narrow resonances is not observed in the measured spectrum can be attributed to the inhomogeneous spectral broadening associated with inherent fabrication imperfections. Interestingly enough, as discussed above, these two resonances were found to be quasi-BICs.

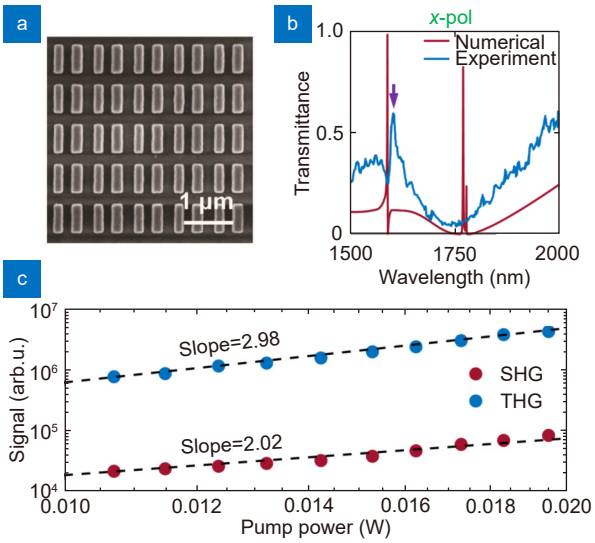

Fig. 5 | (**a**) Top-view SEM image of a fabricated metasurface corresponding to α = 0.075. (**b**) Comparison of experimentally measured linear transmittance and the corresponding numerically calculated spectrum at α = 0.075. The purple arrow denotes the resonance that is used to illustrate the measured power-dependent second-harmonic and third-harmonic signals presented in (c). (**c**) Measured power-dependent output SH (red dots) and TH (blue dots) signals from the fabricated sample with α = 0.075. The dependence of nonlinear emissions is measured at the resonance with (pump) wavelength of 1620 nm under field polarization oriented along the *x*-axis. The dots represent the measured data while the black dashed lines denote the fitting lines of SHG and THG power.

The dependence of the power generated at the SH and TH on the pump power, measured again for the metasurface with $\alpha = 0.075$, is depicted in Fig. 5(c). As illustrated by this figure, the fitted slopes of the curves

corresponding to SH and TH nonlinear optical interactions are 2.02 and 2.98, respectively, which clearly proves their quadratic and cubic dependence on the optical power at the FF, respectively (for pump power lower than 0.02 W, which was the power range where experiments were performed).

Considering the relation between the FF optical field and the SH/TH nonlinear polarizations described by Eqs. (1) and (2), one expects that the intensities of generated second- and third-harmonic are highly dependent on the enhancement of the local linear optical field. In addition, double-resonance mechanisms provide an effective method to further enhance nonlinear optical interactions. However, optical losses in amorphous silicon are large in the working spectral range of SHG (750 – 900 nm) and THG (500 – 600 nm), implying weak coupling between the resonances at the FF and the resonances in the vicinity of the SH/TH. Therefore, we do not provide here the linear transmission spectra at the SH and TH. In turn, we have calculated for both polarizations of plane-wave excitation at α = 0.075 the averaged enhancement of the linear local optical field, defined by the relation $\eta_{\rm E} = \frac{1}{V}\int_V |\boldsymbol{E}(\boldsymbol{\omega};\boldsymbol{r})|/E_0 \mathrm{d}\boldsymbol{r}$, where E_0 is the amplitude of the incident electric field and V is the volume of the bar-shaped resonators (amorphous silicon). The results regarding the enhancement of the local electric field are summarized in Fig. 6.

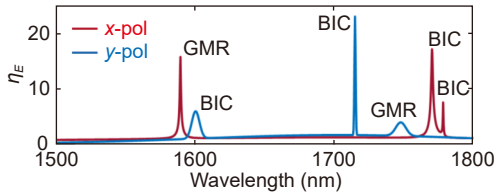

Fig. 6 | Enhancement factor $\eta_{\rm E}$ of the averaged electric field amplitude within the amorphous silicon resonators under plane-wave illumination with the asymmetry of the metasurface being α = 0.075.

Comparing the field enhancement with the Q-factors in Fig. 4, we find that in case of y-polarization, resonances with higher Q-factor correspond to larger linear optical field enhancement. On the other hand, the resonances under x-polarized plane-wave excitation at 1590 nm and 1770 nm possess similar Q-factors and the corresponding enhancement of the linear field is of similar magnitude as well. Moreover, despite its high Q-factor, the enhancement corresponding to the resonance at 1778 nm (x-polarization) is relatively weak due to a smaller amount of field penetrating in the dielectric resonators of the metasurface (see field profile in Fig. 3(h)). Based on the above analysis, we are led to the conclusion that the second-order and third-order nonlinear optical interactions can be analyzed *via* the enhancement of the linear optical field, the Q-factor of the resonances, and the near-field distribution of the GMR and BIC resonances.

After establishing the nature of the nonlinear optical interactions, we turned our attention to a more detailed investigation of the fundamental physics pertaining to the generation of the SH signal. To this end, we first measured the spectral dependence of the SH intensity generated from the dielectric metasurface consisting of bar-shaped meta-atoms, in the case of $\alpha = 0.075$. One key physical quantity that characterizes the spectrum of the generated SH signal is the SH enhancement factor, $\eta_{\rm SHG}$, defined as the ratio between the SH power emitted by the periodic array of dielectric resonators and the SH power generated from an amorphous silicon film of the same thickness. In the case of x-polarized plane-wave pump, three spectral peaks at wavelength of 1620 nm, 1684 nm, and 1714 nm at the fundamental wavelength can be observed in the SHG spectra [see the red curve in Fig. 7(a)]. Importantly, nearly 550 times enhancement of SHG intensity is achieved at the wavelength of 1620 nm, corresponding to the sharp resonance with a large Q-factor, marked by a purple arrow in Fig. 5(b). The additional two spectral resonances observed at longer wavelengths of 1684 and 1714 nm show smaller enhancement factors of 70 and 45, respectively.

To better understand the experimental results, we performed full-wave numerical simulations using the frequency solver of COMSOL Multiphysics and compared the computational results with the experimental data. To facilitate the identification of resonant features in the linear regime, we show in Fig. 7(b) the simulated transmissivity spectra for both polarizations at $\alpha = 0.075$, corresponding to the green dashed lines in Fig. 2(a) and 2(c), the calculations being performed for plane-waves normally incident onto the metasurface. For the nonlinear calculations, nonlinear optical interactions are described by the nonlinear surface and bulk polarizations given by Eq. (1). In this computational analysis, we separated the contributions to the SHG signal of the surface (local) and bulk (nonlocal) nonlinear polarizations, so that we unequivocally can establish which nonlinear optical effect dominates the nonlinear interactions. The results of this analysis are summarized in Fig. 7(c) and 7(d).

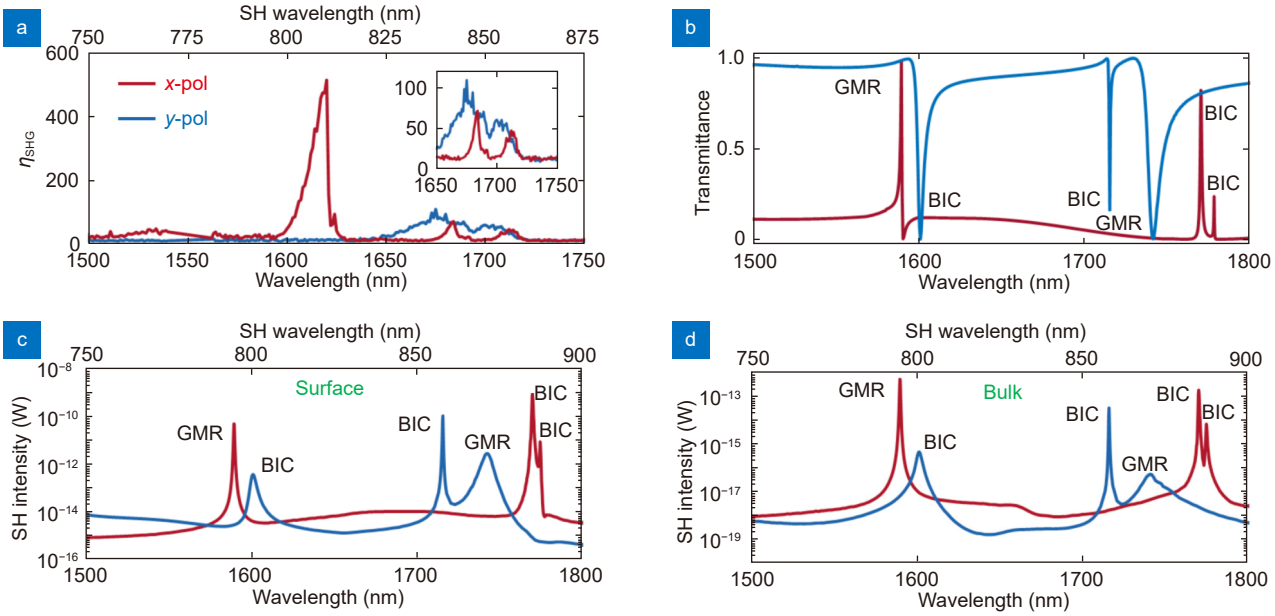

Fig. 7 | (**a**) Measured enhancement factor η_{SHG} of SHG from the all-dielectric metasurface with α = 0.075. An amorphous silicon slab with the same thickness as that of the metasurface is used as a reference. The inset shows a zoom-in of the enhancement factor. (**b**) Simulated linear transmittance for asymmetry parameter α = 0.075. (**c**, **d**) Numerically calculated surface and bulk contributions to SHG, respectively, when α = 0.075. Red (blue) lines correspond *x*-polarized (*y*-polarized)

It can be concluded from these figures that the main spectral features of the experimentally measured spectra are relatively well reproduced. For example, there is only a relative difference of about 2% between the measured and computed wavelengths of the main resonance located at 1620 nm in the measured SHG spectrum.

The comparison between experimental and simulation results reveals several additional ideas: First, the excitation of both the GMR (1620 nm) and quasi-BIC (1684 nm and 1714 nm) resonances produces a large enhancement of the generated SH. Second, the electric-dipole allowed nonlinear polarization is the dominant source of the SHG over almost the entire spectral domain considered in our study. This finding is consistent with the commonly used assumption that the bulk contribution to SHG can be neglected in the case of centrosymmetric materials. Third, there is a difference between the experimental and simulation values of the strength of SH enhancement corresponding to various resonances. These differences can be explained by the reduced experimental values of the *Q*-factors (as extracted from the experimental spectra of η_{SHG}), a decrease attributable to structural perturbations such as fabrication imperfections and finite-size effects. Moreover, whereas in the experiments we measured the SH emitted in the zero-diffraction order, in numerical simulations we computed the total generated SH.

Importantly, despite the fact that the bulk SHG signal is negligible according to our numerically calculated results, the separate incorporation in the simulations of the two sources of SHG provides valuable information regarding the physical properties of the SHG interaction. For example, as per Fig. 7(c), the maximum SH intensity originating from surface effects is observed for the BIC-type resonance located at 1770 nm, whereas the largest value of SH intensity generated in the bulk is found to correspond to the GMR-type resonance located at 1590 nm. One can understand this finding by comparing the near-field distributions corresponding to the two resonances. With this in mind, one can conclude that it is possible to tune the ratio between the surface and bulk contributions to SHG from dielectric metasurfaces made of centrosymmetric optical materials, enabling new tools to use in the design of active photonic nanodevices.

We also measured SHG from the asymmetric metasurface under the condition of a *y*-polarized incident plane wave, the results being presented in Fig. 7(a). Comparing these results with the corresponding simulated spectra shown in Fig. 7(c) and 7(d), we see that again the spectral positions of the two η_{SHG} resonances (quasi-BIC at 1675 nm and GMR at 1700 nm) in the computed and measured spectra agree within a difference of about 2%. Overall, our simulated nonlinear spectra agree well with the measured SHG; however, perhaps due to the

inhomogeneous spectral broadening effects, the resonance at 1600 nm in the computed spectra is not observed in experimentally measured ones. Using as a reference an amorphous silicon film with the same thickness as the metasurface, we determined that the SHG is resonantly enhanced by 110 times at 1675 nm and 70 times at 1700 nm. Similarly, to the case of x-polarized incident plane-waves discussed above, the contribution of the surface term to the SHG dominates when compared to the bulk contribution under y-polarized incident waves. Moreover, the large nonlinear enhancement arises chiefly from high-Q quasi-BIC at 1675 nm and the GMR at 1700 nm.

In addition to second-order nonlinear effects, the proposed resonant metasurface ($\alpha = 0.075$) can also enhance THG arising from the large (bulk) third-order optical nonlinearity of amorphous silicon. To characterize the enhancement effect, we define a TH enhancement factor, η_{THG}, as the ratio between the TH power emitted by the asymmetric metasurface and the TH power generated from an amorphous silicon slab with the same thickness as that of the metasurface. The results of the measurements and the computed THG spectra corresponding to the third-order nonlinear polarization described by Eq. (2), determined under plane-wave excitation at the FH for both x-polarized (red) and y-polarized (blue) incident plane waves, are summarized in Fig. 8. Regarding the case of incident waves polarized along the x-axis, the high-Q GMR-type resonance at the FF wavelength (1620 nm) gives rise to extremely large THG enhancement, namely nearly 4200 times enhancement, whereas the two quasi-BICs originating from the symmetry breaking of the unit cell induce a $\eta_{\mathrm{THG}} = 340$ at 1674 nm and $\eta_{\mathrm{THG}} = 1341$ at 1715 nm. Moreover, the dielectric metasurface under an y-polarized incident wave excitation supports two resonances, namely a quasi-BIC at λ=1675 nm with enhancement factor of $\eta_{\mathrm{THG}} = 3790$ and a GMR at λ=1712 nm with $\eta_{\mathrm{THG}} = 4930$.

Comparing Fig. 8(a) and 8(b) we see that, overall, for both polarizations there is a good agreement between the experimental results and numerically computed spectra characterizing the third-order nonlinear optical response of the asymmetric bar-shaped metasurface. Due to fabrication and structural imperfections, there is a small difference between the resonance wavelengths of the peaks seen in the measured and computed nonlinear enhancement spectra. In addition, due to inhomogeneous spectral broadening, the Q-factor of measured spectral resonances is somewhat smaller than that of the computed spectra (see the quasi-BIC at λ=1675 nm excited by an y-polarized plane-wave). This effect results in a decrease of THG intensity. It should also be noted that despite the fact that the computed spectra for x-polarized incident plane waves display two quasi-BIC resonances at $\lambda \approx 1770$ nm, only one such resonance can be observed experimentally at this frequency. This is so because the two corresponding resonances at the FF merge as the result of inhomogeneous spectral broadening effects induced by fabrication imperfections.

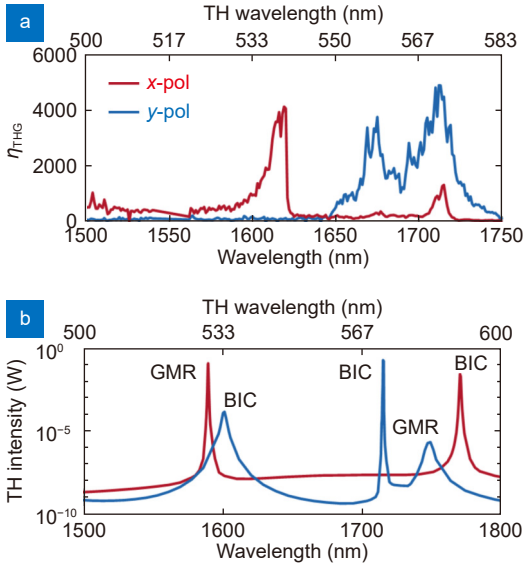

Fig. 8 | (**a**) Measured enhancement factor of THG from the resonant metasurface described by α = 0.075. (**b**) Numerically calculated TH intensity spectra corresponding to the same metasurface. Red (blue) lines correspond to x-polarized (y- polarized) incident plane-waves. In both figures, the upper ticks of the x-axis denote the TH wavelength.

According to our experimental measurements, the up-conversion efficiencies of second-order ($P_{\mathrm{SHG}}/P_{\mathrm{pump}}$) and third-order ($P_{\mathrm{THG}}/P_{\mathrm{pump}}$) nonlinear processes are estimated to be 10^{-8} and 10^{-7}, respectively. To compare these values to the state-of-the-art, we mention that the current record efficiencies are 6.8×10^{-7} for SHG from arrayed silicon slotted nanocubes[41] and 1.8×10^{-6} for THG measured from silicon pillar metasurfaces[57]. Thus, the nonlinear conversion efficiency reported in this work is not record high but comparable to the state-of-the-art.

It is also relevant to consider the directionality of the SHG and THG transmission, since the working wavelengths at SHG and THG are beyond the diffraction limit (1245 nm). To characterize the nonlinear emissions into different diffraction channels, we performed

the Fourier analysis of numerically calculated transmitted nonlinear signals, for the cases of SHG at 1620 nm under x-polarized excitation, which corresponds to the highest measured SHG enhancement, and THG at 1747 nm under y-polarized excitation, which corresponds to the largest measured THG enhancement.

Figure 9 displays the normalized power distribution in each diffraction channel, where m and n denote the orders of diffraction corresponding to the x- and y-directions, respectively. Regarding the SHG (see Fig. 9(a)), our results indicate that 9 diffraction channels exist and the emission angle θ_{SHG} for each of them are: 0° for (0,0) order; 39.7° for (1, 0), (−1, 0), (0, 1) and (0, −1) orders; and 64.6° for (1, 1), (1, −1), (−1, 1) and (−1, -1) orders. Most of the nonlinear power at SH radiates into the (1,0) and (−1, 0) channels, whereas the emission into zeroth order is only about 0.05 of the power emitted in the diffraction order corresponding to the highest emission. Regarding THG, the periodic structure of the metasurface allows 13 diffraction orders at the TH wavelength, and the emission angle θ_{THG} for these diffraction channels are: 0° for (0, 0) order; 27.9° for (1, 0), (−1, 0), (0, 1) and (0, −1) orders; 41.4° for (1, 1), (1, −1), (−1, 1) and (−1, −1) orders; and 69.3° for (2, 0), (−2, 0), (0, 2) and (0, −2) orders. Clearly, most power is emitted in the (0, −2) diffraction order, and compared to this, the THG emission in the zeroth order is about 0.14. All diffraction orders are included in our simulations by integrating the outgoing power flow in the transmission side of the metasurface. In the case of experimental measurements, the nonlinear signals are collected only from the zero-diffraction order.

Importantly from a practical point of view, we have demonstrated in this section both theoretically and experimentally that strong enhancement of several nonlinear optical processes (SHG and THG in our case) can be achieved in the same nonlinear metasurface, which suggests that such photonic nanodevices can become instrumental in designing active optical devices with new or improved functionality.

Dependence of SHG and THG on the metasurface asymmetry

As discussed above from both experimental and computational perspectives, high-Q resonances supported by dielectric metasurfaces make it possible to realize enhanced second- and third-order nonlinear optical interactions. The calculated transmission spectra exhibited in Fig. 2 demonstrate that the linewidth (or Q-factor) of both GMR-type and BIC-type resonances, which determines the local field enhancement, are sensitive to the variation of the asymmetry of the meta-atom. We now go a step further aiming to gain a deeper and more comprehensive insight into the dependence of harmonic generation on the asymmetry features of the dielectric metasurface. To this end, we simulate the nonlinear optical response of the metasurface for different values of α, that is for 0, 0.075, 0.15, and 0.225. Since we observed a good agreement between experimental and simulation data, here we present only results obtained through rigorous simulations of the bar-shaped amorphous silicon metasurface.

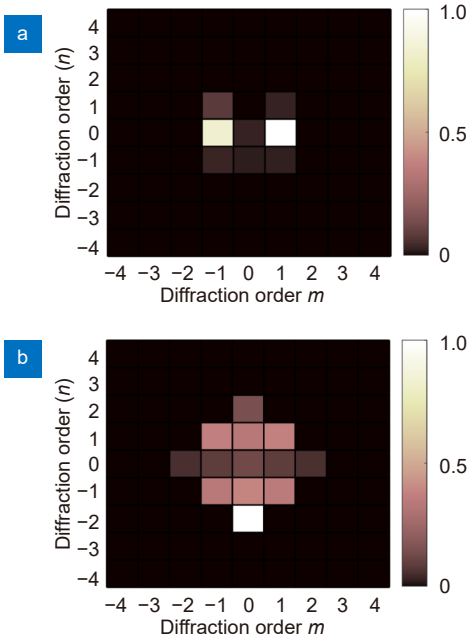

Fig. 9 | Fourier analysis of numerically calculated (**a**) transmitted SHG at 1590 nm (under x-polarized incident plane-wave), which corresponds to the resonant peak of highest measured SHG enhancement, and (**b**) transmitted THG at 1747 nm (under y- polarized incident plane-wave), which corresponds to the resonant peak of largest THG enhancement in experiments. Fourier analysis is performed for an asymmetry parameter of α = 0.075.

The simulated SHG spectra presented in Fig. 10 reveal that the resonance wavelength and the linewidth of the corresponding resonances vary considerably with the asymmetry parameter, α. Comparing the two contributions to SHG, we can infer that for both polarizations and for all values of α, the surface contribution to the SHG is much larger than that of the bulk term. It is worth noting that in the case of $\alpha = 0$, BICs are completely uncoupled with the radiation continuum and manifest themselves as spectral peaks with vanishingly

small width [see the red lines depicting the SHG intensity spectra in Fig. 10(a–d)]. As α increases, due to the introduced structural asymmetry, the BICs are no longer symmetry-protected, which results in a strong optical coupling between the localized modes and the extended propagating waves. The signature of this strong optical interaction is the appearance of sharp resonances in the nonlinear response spectra. Furthermore, the results of the eigenmode analysis presented in Fig. 4 show that the *Q*-factors of BIC-type resonances decrease with the asymmetry parameter. Importantly, an opposite trend is observed in the case of the GMR-type resonances, namely their *Q*-factors slowly increase when the asymmetry parameter increases. It is expected therefore that the corresponding surface and bulk SHG present a similar dependence on the structural asymmetry. To confirm this conjecture, for both polarizations we analyze the dependence of each resonance of the metasurface on the asymmetry parameter α. As can be seen in Fig. 10(a–d), indeed the width of the SHG resonances corresponding to quasi-BICs gradually increases with the increase of asymmetry parameter, whereas the opposite is true in the case of GMR resonances.

Finally, we investigated the relationship between the asymmetry parameter and the efficiency of the THG process. The corresponding simulated results are plotted in Fig. 11, where a strong dependence of TH intensity on the asymmetry parameter α can be clearly observed for plane-wave excitation at the FF wavelength with the field polarized along either *x*- or *y*-axis. Comparing these results with the SHG spectra in Fig. 10, one can draw conclusions similar to those valid in the case of SHG: First, both quasi-BICs and GMR-type resonances with large *Q*-factors induce greatly enhanced TH nonlinear signals. Second, the spectral location of resonances at the TH intensity, corresponding to different values of the asymmetry parameter α, are closely related to the resonances at the FF. Third, the width of BIC-induced resonances at TH increases with the asymmetry of the metasurface, whereas the opposite trend is observed at the resonance wavelengths corresponding to excitation of GMR-type resonances. We also note that in the experimental

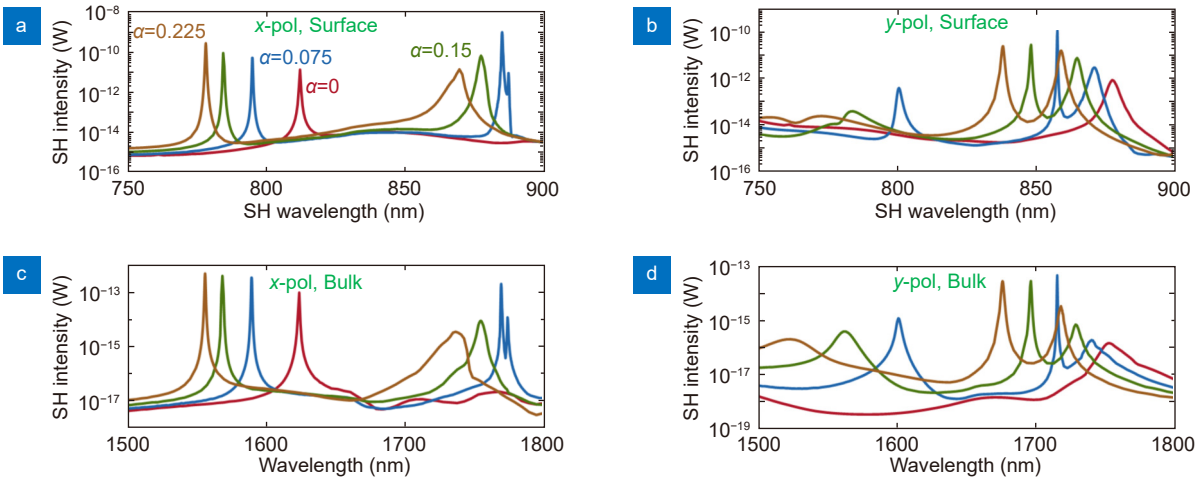

Fig. 10 | Simulated dependence of SHG from the amorphous silicon metasurface with respect to the structural asymmetry parameters α in cases of (**a**) surface contribution under *x*-polaried excitation, (**b**) surface contribution under *y*-polarized excitation, (**c**) bulk contribution under *x*-polarized excitation, and (**d**) bulk contribution under *y*-polarized excitation.

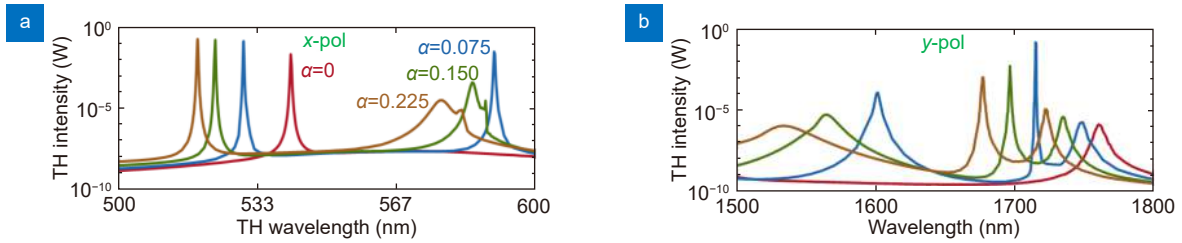

Fig. 11 | Numerical simulation of asymmetry-dependent TH intensity under plane wave excitation with polarization along (**a**) *x* and (**b**) *y* directions, respectively. In both figures, the upper ticks of the *x*-axis denote the TH wavelength.

samples both SHG and THG efficiency dependence on the asymmetry is affected by the ratio of the radiative and other types of losses. The maximal enhancement can be usually achieved in the critical coupling regime[40].

Conclusion

We have demonstrated a promising way to enhance and engineer the second- and third-order nonlinear optical response from an all-dielectric metasurface with a unit cell possessing broken in-plane symmetry, utilizing the physics of high-Q guided mode resonances and symmetry-protected bound states in the continuum. We have experimentally demonstrated that the proposed amorphous silicon metasurface can induce nearly 550 times second-harmonic generation enhancement and a 5000-fold enhancement of third-harmonic generation in the case when the asymmetry parameter $\alpha = 0.075$. Remarkably, we have also numerically examined the asymmetry dependence of second-harmonic generation (surface and bulk terms) and third-harmonic generation (bulk term) from centrosymmetric amorphous silicon and provided a comprehensive investigation of the contribution of different sources of optical nonlinearity to second-harmonic and third-harmonic generation in the proposed all-dielectric metasurface. We believe that our work is particularly significant to the development of new methods for achieving enhanced nonlinear optical interactions at the nanoscale and to effectively manipulate higher-harmonic generation in dielectric structures made of centrosymmetric materials, thus enabling novel photonic applications and devices with new or improved functionalities.

References

1. Yu NF, Capasso F. Flat optics with designer metasurfaces. *Nat Mater* **13**, 139–150 (2014).
2. Chen HT, Taylor AJ, Yu NF. A review of metasurfaces: physics and applications. *Rep Prog Phys* **79**, 076401 (2016).
3. Li GX, Zhang S, Zentgraf T. Nonlinear photonic metasurfaces. *Nat Rev Mater* **2**, 17010 (2017).
4. Zheludev NI, Kivshar YS. From metamaterials to metadevices. *Nat Mater* **11**, 917–924 (2012).
5. Kadic M, Milton GW, van Hecke M et al. 3D metamaterials. *Nat Rev Phys* **1**, 198–210 (2019).
6. Yang Y, Seong J, Choi M et al. Integrated metasurfaces for re-envisioning a near-future disruptive optical platform. *Light Sci Appl* **12**, 152 (2023).
7. Beruete M, Jáuregui-López I. Terahertz sensing based on metasurfaces. *Adv Opt Mater* **8**, 1900721 (2020).
8. Qin J, Jiang SB, Wang ZS et al. Metasurface micro/nano-optical sensors: principles and applications. *ACS Nano* **16**, 11598–11618 (2022).
9. Li LL, Cui TJ, Ji W et al. Electromagnetic reprogrammable coding-metasurface holograms. *Nat Commun* **8**, 197 (2017).
10. Li X, Zhang X, Zhao RZ et al. Independent light field manipulation in diffraction orders of metasurface holography. *Laser Photonics Rev* **16**, 2100592 (2022).
11. Krasnok A, Tymchenko M, Alù A. Nonlinear metasurfaces: a paradigm shift in nonlinear optics. *Mater Today* **21**, 8–21 (2018).
12. Huang TY, Zhao X, Zeng SW et al. Planar nonlinear metasurface optics and their applications. *Rep Prog Phys* **83**, 126101 (2020).
13. Liu S, Sinclair MB, Saravi S et al. Resonantly enhanced second-harmonic generation using III-V semiconductor all-dielectric metasurfaces. *Nano Lett* **16**, 5426–5432 (2016).
14. Sarma R, Xu JM, de Ceglia D et al. An all-dielectric polaritonic metasurface with a giant nonlinear optical response. *Nano Lett* **22**, 896–903 (2022).
15. Zheng Z, Xu L, Huang LJ et al. Third-harmonic generation and imaging with resonant Si membrane metasurface. *Opto-Electron Adv* **6**, 220174 (2023).
16. Smirnova D, Kruk S, Leykam D et al. Third-harmonic generation in photonic topological metasurfaces. *Phys Rev Lett* **123**, 103901 (2019).
17. Zograf G, Koshelev K, Zalogina A et al. High-harmonic generation from resonant dielectric metasurfaces empowered by bound states in the continuum. *ACS Photonics* **9**, 567–574 (2022).
18. Panoiu NC, Sha WEI, Lei DY et al. Nonlinear optics in plasmonic nanostructures. *J Opt* **20**, 083001 (2018).
19. Bin-Alam MS, Reshef O, Mamchur Y et al. Ultra-high-Q resonances in plasmonic metasurfaces. *Nat Commun* **12**, 974 (2021).
20. Arbabi A, Horie Y, Bagheri M et al. Dielectric metasurfaces for complete control of phase and polarization with subwavelength spatial resolution and high transmission. *Nat Nanotechnol* **10**, 937–943 (2015).
21. Hu YQ, Wang XD, Luo XH et al. All-dielectric metasurfaces for polarization manipulation: principles and emerging applications. *Nanophotonics* **9**, 3755–3780 (2020).
22. Fan SH, Joannopoulos JD. Analysis of guided resonances in photonic crystal slabs. *Phys Rev B* **65**, 235112 (2002).
23. Quaranta G, Basset G, Martin OJF et al. Recent advances in resonant waveguide gratings. *Laser Photonics Rev* **12**, 1800017 (2018).
24. Jang J, Badloe T, Yang Y et al. Spectral modulation through the hybridization of mie-scatterers and quasi-guided mode resonances: realizing full and gradients of structural color. *ACS Nano* **14**, 15317–15326 (2020).
25. Lawrence M, Barton III DR, Dixon J et al. High quality factor phase gradient metasurfaces. *Nat Nanotechnol* **15**, 956–961 (2020).
26. Huang LJ, Jin R, Zhou CB et al. Ultrahigh-Q guided mode resonances in an All-dielectric metasurface. *Nat Commun* **14**, 3433 (2023).
27. Yuan S, Wu YK, Dang ZZ et al. Strongly enhanced second harmonic generation in a thin film lithium niobate heterostructure cavity. *Phys Rev Lett* **127**, 153901 (2021).
28. Gigli C, Leo G. All-dielectric $\chi^{(2)}$ metasurfaces: recent progress. *Opto-Electron Adv* **5**, 210093 (2022).
29. Zhao Y, Chen ZX, Wang C et al. Efficient second- and higher-order harmonic generation from $LiNbO_3$ metasurfaces. *Nanoscale* **15**, 12926–12932 (2023).

30. Marinica DC, Borisov AG, Shabanov SV. Bound States in the continuum in photonics. *Phys Rev Lett* **100**, 183902 (2008).
31. Hsu CW, Zhen B, Stone AD et al. Bound states in the continuum. *Nat Rev Mater* **1**, 16048 (2016).
32. Koshelev K, Bogdanov A, Kivshar Y. Meta-optics and bound states in the continuum. *Sci Bull* **64**, 836–842 (2019).
33. Azzam SI, Kildishev AV. Photonic bound states in the continuum: from basics to applications. *Adv Opt Mater* **9**, 2001469 (2021).
34. Sadrieva ZF, Sinev IS, Koshelev KL et al. Transition from optical bound states in the continuum to leaky resonances: role of substrate and roughness. *ACS Photonics* **4**, 723–727 (2017).
35. Koshelev K, Lepeshov S, Liu MK et al. Asymmetric metasurfaces with high-*Q* resonances governed by bound states in the continuum. *Phys Rev Lett* **121**, 193903 (2018).
36. Huang C, Zhang C, Xiao SM et al. Ultrafast control of vortex microlasers. *Science* **367**, 1018–1021 (2020).
37. Wang B, Liu WZ, Zhao MX et al. Generating optical vortex beams by momentum-space polarization vortices centred at bound states in the continuum. *Nat Photonics* **14**, 623–628 (2020).
38. Yu ZJ, Xi X, Ma JW et al. Photonic integrated circuits with bound states in the continuum. *Optica* **6**, 1342–1348 (2019).
39. Bykov DA, Bezus EA, Doskolovich LL. Bound states in the continuum and strong phase resonances in integrated Gires-Tournois interferometer. *Nanophotonics* **9**, 83–92 (2020).
40. Koshelev K, Tang YT, Li KF et al. Nonlinear metasurfaces governed by bound states in the continuum. *ACS Photonics* **6**, 1639–1644 (2019).
41. Fang CZ, Yang QY, Yuan QC et al. Efficient second-harmonic generation from silicon slotted nanocubes with bound states in the continuum. *Laser Photonics Rev* **16**, 2100498 (2022).
42. Hong PL, Xu L, Rahmani M. Dual bound states in the continuum enhanced second harmonic generation with transition metal dichalcogenides monolayer. *Opto-Electron Adv* **5**, 200097 (2022).
43. Sinev IS, Koshelev K, Liu ZJ et al. Observation of ultrafast self-action effects in quasi-BIC resonant metasurfaces. *Nano Lett* **21**, 8848–8855 (2021).
44. Koshelev K, Tang YT, Hu ZX et al. Resonant chiral effects in nonlinear dielectric metasurfaces. *ACS Photonics* **10**, 298–306 (2023).
45. COMSOL Multiphysics. Available from: https://www.comsol.com.
46. Synopsys' RSoft Photonic Device Tools. Available from: https://www.synopsys.com/photonic-solutions/rsoft-photonic-device-tools/rsoft-products.html.
47. Pierce DT, Spicer WE. Electronic structure of amorphous si from photoemission and optical studies. *Phys Rev B* **5**, 3017–3029 (1972).
48. CDGM Zemax catalog 2022–06. Available from: http://www.cdgmgd.com.
49. Heinz TF. Second-order nonlinear optical effects at surfaces and interfaces. *Mod Probl Condens Matter Sci* **29**, 353–416 (1991).
50. Timbrell D, You JW, Kivshar YS et al. A comparative analysis of surface and bulk contributions to second-harmonic generation in centrosymmetric nanoparticles. *Sci Rep* **8**, 3586 (2018).
51. Falasconi M, Andreani LC, Malvezzi AM et al. Bulk and surface contributions to second-order susceptibility in crystalline and porous silicon by second-harmonic generation. *Surf Sci* **481**, 105–112 (2001).
52. Corvi M, Schaich WL. Hydrodynamic-model calculation of second-harmonic generation at a metal surface. *Phys Rev B* **33**, 3688–3695 (1986).
53. Guyot-Sionnest P, Chen W, Shen YR. General considerations on optical second-harmonic generation from surfaces and interfaces. *Phys Rev B* **33**, 8254–8263 (1986).
54. Sipe JE, So VCY, Fukui M et al. Analysis of second-harmonic generation at metal surfaces. *Phys Rev B* **21**, 4389–4402 (1980).
55. Grillet C, Carletti L, Monat C et al. Amorphous silicon nanowires combining high nonlinearity, FOM and optical stability. *Opt Express* **20**, 22609–22615 (2012).
56. Han S, Rybin MV, Pitchappa P et al. Guided-mode resonances in all-dielectric terahertz metasurfaces. *Adv Opt Mater* **8**, 1900959 (2020).
57. Yang GC, Dev SU, Allen MS et al. Optical bound states in the continuum enabled by magnetic resonances coupled to a mirror. *Nano Lett* **22**, 2001–2008 (2022).

Acknowledgements

The work in Canberra was supported by the Australian Research Council (Grant No. DP210101292) and the International Technology Center Indo-Pacific (ITC IPAC) *via* Army Research Office (contract FA520923C0023).

Author contributions

Y. Kivshar and N. C. Panoiu conceived the idea and supervised the research. J. T. Wang performed numerical simulations. K. Koshelev designed the metasurface. F. X. Lai and Q. H. Song fabricated the metasurfaces. P. Tonkaev and S. Kruk conducted nonlinear experiments and processed data from them. All authors contributed to the manuscript writing and participated in the discussions.

Competing interests

The authors declare no competing financial interests.